X International Conference on Computational Methods for Coupled Problems in Science and Engineering
COUPLED PROBLEMS 2023
M. Papadrakakis, B. Schrefler and E. Oñate (Eds)

FLUID-STRUCTURE INTERACTION MODEL OF DRY WIRE DRAWING WITH COUPLED AXIAL VELOCITY AND LAYERING

MATHIEU VERVAECKE[1,*], DIETER FAUCONNIER[2,3] AND JORIS DEGROOTE[1,3]

[1] Department of Electromechanical, Systems and Metal Engineering, Ghent University
Sint-Pietersnieuwstraat 41, 9000 Ghent, Belgium
e-mail: Mathieu.Vervaecke@UGent.be

[2] Department of Electromechanical, Systems and Metal Engineering, Ghent University
Technologiepark Zwijnaarde 46, 9052 Zwijnaarde, Belgium

[3] Flanders Make MIRO, Ghent, Belgium

Key words: Wire drawing, Fluid-Structure Interaction (FSI), OpenFOAM, Mesh motion

Abstract. An innovative 2D axisymmetric fluid-structure interaction model of wire drawing is developed to numerically investigate the interaction between the thin lubricant film and the plastically deforming steel wire. The deformation of the wire is obtained from the linear momentum balance and the lubricant film has been calculated by the Navier-Stokes equations. Moreover, the coupling between wire and lubricant is performed by the IQN-ILS technique and a no-slip condition is imposed on the sliding fluid-structure interaction interface. In order to reduce the computational cost, a layering technique is implemented in the axially moving structure domain. This results on the one hand in monitoring the stresses and displacements of the structure and on the other hand in an observation of the hydrodynamic pressure build-up and wall shear stresses in the lubricant. Additionally, the evolution of the fluid film thickness is presented.

1 INTRODUCTION

Dry wire drawing is a cold work hardening process employed to progressively reduce the cross-section of a wire by pulling it through a series of dies. The use of a sodium or calcium-based soap lubricant in dry wire drawing is essential to reduce the drawing forces and the corresponding power. Moreover, the thin lubricant film separates the surfaces of the wire and the die, which enlarges the service life of the die.

Optimization of a metal forming process, such as wire drawing, often involves a costly and time-consuming trial-and-error based experimental methodology. However, by using a numerical model of the metal forming process, the number of experiments can be reduced. When modeling the dry wire drawing process the elastoplastic deformation of the metal wire needs to be considered, while the die is approximated as a rigid body [1, 2]. The thin lubricant film is typically determined using the Reynolds equation [1], which has been generalized to incorporate variable density and viscosity. Moreover, this equation is able to adequately capture the mechanics of a piezo-viscous lubricant if $\tau\alpha > 1$ [3]. However, in a wire drawing process, this condition is not satisfied as the shear stress τ can exceed values of $10^8 Pa$, whereas $10^{-8} Pa^{-1}$ is a conservative value of pressure-viscosity coefficient

α. Hence the Navier-Stokes equations are used to more accurately capture the piezo-viscous behavior of the soap in the future [3, 4]. However, in this ongoing study a high constant value of the viscosity is assumed to avoid die-wire contact during the simulation. The piezo-viscous and shear-thinning behavior of the lubricant as well as the temperature effects will be implemented and investigated in a later phase.

A first attempt to simulate the dry wire drawing process with strongly coupled partitioned fluid-structure interaction (FSI) and sliding interface was presented in [4]. The lubricant film was calculated by the Navier-Stokes equations and the wire deformation was obtained from the linear momentum balance [6]. To restrict a high computational cost of the simulation, the length of the wire was limited in this attempt. Consequently, it prevented this model from achieving steady-state results. Moreover a constant velocity was imposed at the interface of the lubricant contacting the wire, which ignores the reduction in cross-section.

To achieve a steady-state result and a decrease in computational cost, current work presents the implementation of a *layering* technique on the axially moving structure [7]. Furthermore, the implementation of a *no-slip* condition on the sliding interface is outlined by coupling the axial velocity of the wire with that of the lubricant [8]. Combining the layering technique with the no-slip condition initially caused oscillations of the radial displacement of the moving structure and consequently of the velocity along the wire, which prevented convergence of the FSI method. The origin of these oscillations is discussed and a solution is provided.

2 METHODOLOGY

This section presents the geometry, boundary conditions and settings of the wire drawing case, including a brief description of the implementation of the layering technique on the structural side. Additionally, the applied FSI, fluid and structure solver are outlined. Moreover, the FSI subsection discusses the implementation of the no-slip condition on the interface of this model.

2.1 Geometry, boundary conditions and settings

During a dry wire drawing process the metal wire passes through a stationary reservoir for soap granules, from which soap is entrained and squeezed between the moving wire and the stationary die (Figure 1). In the presented axisymmetric model, the stationary soap reservoir is not taken into account and the lubricant is approximated as a fluid from the onset. Atmospheric pressure is imposed at the inlet and outlet of the lubricant domain. Figure 1 illustrates the starting position of the wire drawing simulation. It consists of an originally undeformed wire, which passes through a die with an initially enlarged diameter. As shown in Figure 1 the space between the wire and the die is represented by the lubricant having a predefined film thickness. During the simulation, the die diameter decreases gradually until it reaches its real diameter, while the wire passes through the die and deforms until a new wire radius is reached. Figure 2 represents a steady-state model, with correct die diameter. Consequently, the die is approximated as a body with prescribed deformation, while the elastoplastic deformation of the wire is calculated.

In comparison with [4], the wire is significantly shorter, due to the used layering technique for the structure. The deformations are thus only calculated in the area of interest, ensuring a lower computational cost. As presented in Figure 2, this layering technique involves the removal of the deformed layer of cells on the right side of the structural domain, whereas a new layer of cells is added to the

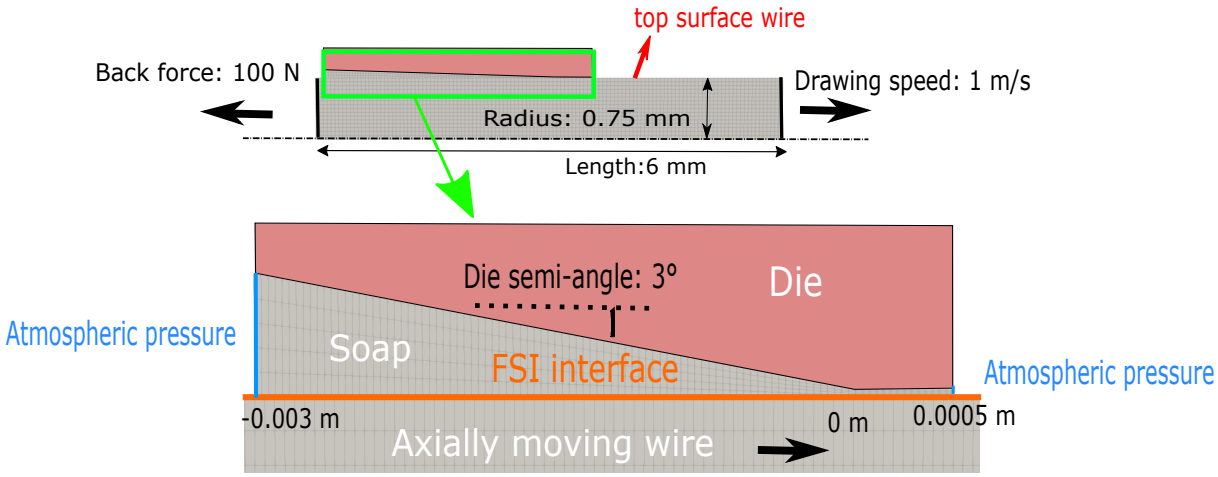

Figure 1: Axisymmetric wire-die configuration at initial condition, close up is 5 times scaled in radial direction

undeformed wire on the left side of the structural domain.

A constant axial drawing velocity of 1 m/s is applied on the right end of the wire. The axial velocity of the lubricant is coupled with the axial top surface velocity of the wire (Figure 1), which preserves the no-slip condition between the wire and the boundary of the lubricant contacting the wire. Furthermore, a back force of 100 N is applied.

Table 1: Mechanical properties of the wire

Young's modulus	E	177GPa
Density	ρ	7833 kg/m³
Poisson coefficient	υ	0.3
Initial yield stress	σ_y	1.25GPa
Hardening coefficient		0.3

The mechanical properties of the wire are specified in Table 1. Following [4], the wire diameter is 1.5 mm and the die angle is 6°. Additionally, a constant lubricant viscosity of 350 Pas is applied. Table 2 gives the settings concerning the numerical calculations. The case is solved for time t = [0s, 0.051s]. During the first 20 time steps the die has the artificially enlarged diameter to avoid numerical

Table 2: Numerical settings

Number of cells wire	1952
Number of cells lubricant	500
Number of faces wire on FSI interface	76
Number of faces lubricant on FSI interface	100
Absolute tolerance FSI coupling	0.005 µm
Time step (Δt)	0.00005 s
Total number of time steps	1015
Time steps before shrinking die diameter	20
Time steps during shrinking die diameter	900

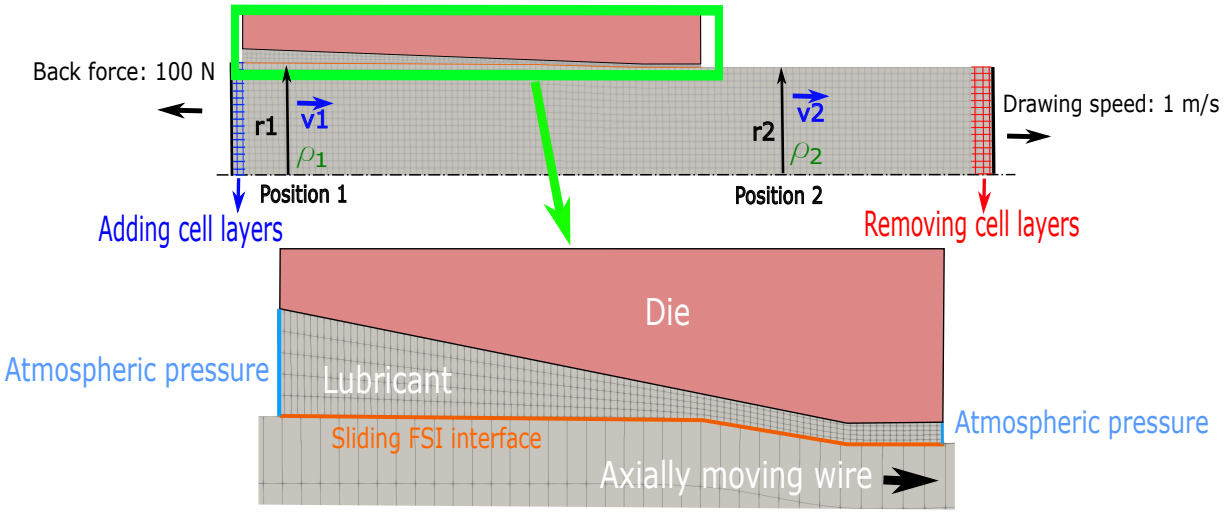

Figure 2: Axisymmetric wire-die configuration at steady state, close up is 5 times scaled in radial direction

instabilities, caused by the acceleration of the wire from 0 to 1 m/s. After these 20 time steps the die diameter starts to shrink each time step until reaching the actual die diameter at time step 920, where a maximum cross-section reduction of 9% of the wire is achieved.

2.2 Solvers

Following [4], a cell-centered finite volume discretization using pimpleFoam [5] has been adopted to model the fluid. A Lagrangian solver in OpenFOAM-extend executes the structural calculations [6]. The in-house FSI coupling code CoCoNuT performs the coupling of the flow solver and structural solver by using the quasi-Newton IQN-ILS technique [8, 9].

2.2.1 FSI solver

In general, an FSI problem exists of a structural domain Ω_s and a fluid domain Ω_f. The boundaries of both domains are indicated as Γ_s and Γ_f, respectively. Figure 1 and 2 present the FSI interface of the model, which is the intersection of the structure and fluid boundaries and is denoted as $\Gamma_i = \Gamma_s \bigcap \Gamma_f$. In order to obtain an FSI solution, the kinematic and the dynamic condition have to be fulfilled [9]. The kinematic condition is defined as

$$\vec{v_f} = \frac{D\vec{u_s}}{Dt} \tag{1}$$

for all points on the interface, with the fluid velocity $\vec{v_f}$ and the structural displacement given by $\vec{u_s}$. Furthermore, the dynamic condition is the equality of the traction at the interface, but opposite in sign

$$\sigma_f \cdot \vec{n_f} = -\sigma_s \cdot \vec{n_s}, \tag{2}$$

with σ is the stress tensor and $\vec{n}$ is the unit normal vector pointed outwards from the domain. The flow and structure solver are briefly written by $F(x)$ and $S(y)$, respectively. The displacements of the grid points on the interface are represented by x, while y gives the loads on the fluid-structure interface. The output of a solver is denoted with a tilde.

$$\widetilde{y}_{k+1} = F(x_{k+1}) \tag{3}$$

$$\widetilde{x}_{k+1} = S(y_{k+1}) \tag{4}$$

The coupling iteration is represented by $k+1$. To obtain sufficient quality of the FSI interface, mapping is required. The mapping blocks M_{FS} and M_{SF} execute the required transfer of data from the fluid domain to the structure domain and the other way around, respectively. The mapping blocks contain a bidirectional linear interpolation between the structural and fluid grid. Algorithm 1 presents the solution procedure of modeling wire drawing with FSI.

Algorithm 1 Solution procedure FSI calculation wire drawing

1: **for** all time steps **do**
2: k = 0
3: $\widetilde{y}_0 = F(x_0)$
4: $y_0 = M_{FS}(\widetilde{y}_0)$
5: $\widetilde{x}_0 = S(y_0)$ ▷ See algorithm 2
6: $r_0 = \widetilde{x}_0 - x_0$
7: **while** $\|r_k\|_2 > \varepsilon_x$ **do**
8: $x_{k+1} = x_k + \Delta x_k^{IQN}$
9: $\widetilde{y}_{k+1} = F(x_{k+1})$
10: $y_{k+1} = M_{FS}(\widetilde{y}_{k+1})$
11: $\widetilde{x}_{k+1} = S(y_{k+1})$ ▷ See algorithm 2
12: $r_{k+1} = M_{SF}(\widetilde{x}_{k+1}) - x_{k+1}$
13: $k++$
14: **end while**
15: *Update yield stress structure* ▷ [6]
16: *Update mesh structure* ▷ [6]
17: **end for**

Line 8 in Algorithm 1 states that the quasi-Newton IQN-ILS is used as FSI-solver. Furthermore, the residual r of the FSI-loop is calculated as

$$r_{k+1} = \widetilde{x}_{k+1} - x_{k+1} \tag{5}$$

Convergence is reached when $\|r\|_2 \leq \varepsilon_x$, with ε_x the absolute convergence tolerance, which is equivalent to an accuracy of 0.005 µm on the radial displacement of the wire (Table 2).

During the simulation, the lubricant domain Ω_f stays fixed in axial direction, while the wire domain Ω_s moves along the axis (Figure 1 and 2). This creates a large translation of the structural mesh with respect to the fluid grid in axial direction. Consequently, a sliding FSI interface approach is applied [4]. This means only the grid velocity normal to the interface has to be the same on both sides of the interfaces [8]. However, to capture the physics of this case a no-slip condition has been implemented on the sliding interface, which means the normal and the tangential material velocity have to be identical in the lubricant and wire at the interface. The implementation of the no-slip condition consists of a transfer of the wire's axial velocity to the fluid boundary contacting the wire. As the axial velocity is 5 orders of magnitude higher than the radial displacement of the wire, it will influence the calculation of the residual significantly. To limit this effect, the axial velocity of the wire has to be divided by 10^5 before transferring the data to the fluid side. Obviously, before imposing the axial velocity on the lubricant boundary contacting the structure, the axial velocity has to be multiplied by 10^5.

2.2.2 CFD

During the simulations the mesh of the fluid film will deform and hence the Arbitrary-Euler-Lagrange (ALE) formulation is used. The conservation of mass and the momentum equations are given by

$$\frac{\partial}{\partial t}\int_{V_f}\rho_f \,\mathrm{d}V_f + \oint_{S_f}\rho_f(\vec{v}_f - \vec{v}_{fg})\cdot\vec{n}_f \,\mathrm{d}S_f = 0 \tag{6}$$

$$\frac{\partial}{\partial t}\int_{V_f}\rho_f\vec{v}_f \,\mathrm{d}V_f + \oint_{S_f}(\rho_f\vec{v}_f \otimes (\vec{v}_f - \vec{v}_{fg}))\cdot\vec{n}_f \,\mathrm{d}S_f = \oint_{S_f}\sigma_f\cdot\vec{n}_f \,\mathrm{d}S_f \tag{7}$$

where V_f is the volume and S_f the surface of the cell. The flow velocity is represented by $\vec{v}_f$, $\vec{v}_{fg}$ is the grid velocity, ρ_f the fluid density and t the time.

A detailed description of the applied discretization schemes of the fluid solver is presented in [4].

To couple the axial velocity of the wire and the fluid boundary contacting the wire, a new boundary condition has been developed in the fluid software. It imposes the axial velocity of the wire on the correct position of the fluid boundary contacting the moving structure.

2.2.3 CSM

Originally, the structural solver was created for simulation of metal forming processes without fluid interaction [6]. During the wire drawing process, work hardening occurs. Consequently, to calculate a correct true stress, the yield stress and the mesh deformation have to be updated each time step. During an FSI calculation, the yield stress field and structural mesh are updated after the coupling iteration have reached the convergence criterion (Algorithm 1, line 18 and 19). A complete explanation of the discretization schemes of the structural solver is presented in [4, 6]. Algorithm 2 presents the structural solver solution procedure for each coupling iteration. The residual r_s of the structural solver is calculated by

$$r_s = \frac{\|\Delta\vec{u}_s^{\,e} - \Delta\vec{u}_s^{\,e-1}\|_\infty}{\|\Delta\vec{u}_s^{\,e}\|_\infty} \tag{8}$$

where e and $e-1$ are the current and previous structural solver iterations, respectively. Convergence is reached when $r_s \leq \zeta$. As the tolerance of the FSI calculation is equal to 0.005 µm, the convergence criterion of the structural solver has to be more strict. Consequently, the convergence tolerance ζ is set to 0.0001 µm.

Algorithm 2 Solution procedure structural solver

```
1: for each FSI-coupling iteration do
2:     while ζ is not reached do
3:         Momentum equation: assemble and solve in terms of Δu_s [6]
4:         Calculate kinematics and stress [6]
5:         Calculate r_s
6:     end while
7:     Update density and equivalent Cauchy stress
8:     Interpolate cell-centre displacements to the vertices
9: end for
```

2.3 Oscillating behavior caused by coupling the axial velocity

Considering the wire drawing model presented in Figure 2, the structural continuity equation at steady-state is given by

$$\rho_1 r_1^2 \vec{v}_1 = \rho_2 r_2^2 \vec{v}_2 \tag{9}$$

where ρ represent the wire density, $\vec{v}$ the speed of the wire and r the radius of the wire. The left side of Equation 9 is represented by the values of *position 1* in Figure 2, while *position 2* of Figure 2 displays the values of the right side of Equation 9. According to Table 1 and Figure 2, ρ_1, $\vec{v}_2$ and r_1 have constant values during the simulation. As deformation of the metal structure occurs during the wire drawing process, $\vec{v}_1 \neq \vec{v}_2$ (Equation 9). Rearranging the terms of Equation 9 with velocity $\vec{v}_1$, which represents the wire speed before deformation, to be solved in the left term results in

$$\vec{v}_1 = \frac{\rho_2}{\rho_1} \frac{r_2^2}{r_1^2} \vec{v}_2 \tag{10}$$

According to Equation 10 the inlet velocity $\vec{v}_1$ depends on the ratio between the densities and the square of the radii multiplied by $\vec{v}_2$. Moreover, Figure 3 outlines the radial displacement of two consecutive time steps n and $n+1$, exposed to a constant pressure distribution. It illustrates that few data points across the width of the lubrication pressure peak are available to impose the load on the moving wire mesh. Consequently, small undesirable differences in radial direction and density occur between two consecutive time steps. This influences the velocity $\vec{v}_1$ (Equation 10) and causes small oscillations of the velocity profile at the inlet of the wire during the simulation (Figure 2). Additionally, these oscillations are detrimental for the convergence of the FSI algorithm.

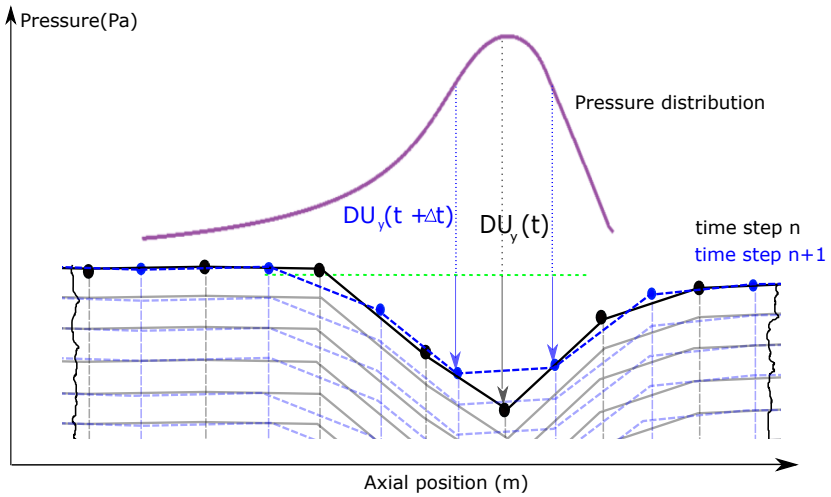

Figure 3: Radial displacement of consecutive time steps subject to a constant load in a discretized system

The most obvious solution is to refine the mesh. However, the computational cost increases significantly by this approach. Moreover, the amplitude of the oscillations is reduced, but they do not disappear. The chosen solution is adding a layer of cells at the left side of the structural domain each time step. This means the location of the cell in current time step is the same as the position of the

preceding cell in previous time step of the axially moving structure. Consequently, each cell experiences an identical load as the preceding cells on that position (Figure 3). This gives an identical radial displacement and density for each time step, which stabilizes the velocity $\vec{v}_1$ (Equation 10). Moreover, the oscillating behavior of the radial displacement disappears and a converged FSI solution can be achieved.

3 RESULTS

The results section first describes the physical effect of the no-slip condition of the model compared with the slip behavior at the steady-state condition. Additionally, the numerical performance is outlined. Figure 4 presents the speed at the top surface of the wire and the velocity imposed on the boundary of the lubricant contacting the wire. It demonstrates a different velocity profile of the lubricant between the slip and no-slip condition. As the slip condition imposes a constant velocity of 1 m/s on the lubricant boundary contacting the wire, a difference is noticed between the structural velocity and the corresponding lubricant speed. As opposed to slip, the no-slip condition presents a perfect fit of the wire velocity and the lubricant velocity. Moreover, the conservation of mass effect on the wire velocity, as stated in Equation 10, is clearly illustrated in Figure 4. It demonstrates the acceleration of the wire speed during the deformation of the wire.

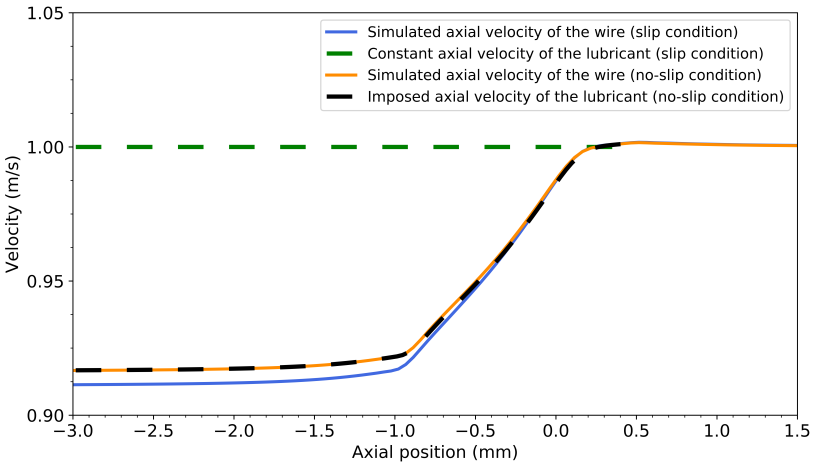

Figure 4: Velocity profile of the wire and corresponding speed imposed on the lubricant boundary contacting the wire, slip vs. no-slip

Another important consequence of applying no-slip is the resulting drawing force of the model at steady-state. The model calculates a force of *201 N* when slip is applied, while *220 N* is achieved after the implementation of no-slip. This presents a significant difference of 8% and indicates the importance of applying no-slip. Consequently, only the results obtained by the no-slip condition will be discussed in the remainder of this section.

Figure 5 presents the equivalent Cauchy stress evolution at the top surface of the wire and the corresponding yield stress during the steady wire drawing modeling. The equivalent Cauchy stress is basically a scalar quantity representing the magnitude of stress. Additionally, Figure 5 illustrates the plastic deformation of the wire, while it is pulled through the die. The steep increase of the equivalent Cauchy stress is limited by the yield stress, which is the point where the wire starts to deform plastically. Moreover, the yield stress and equivalent Cauchy stress increase slightly and work hardening

on the wire occurs. When the wire leaves the die, the equivalent Cauchy stress relaxes and the yield stress stays constant.

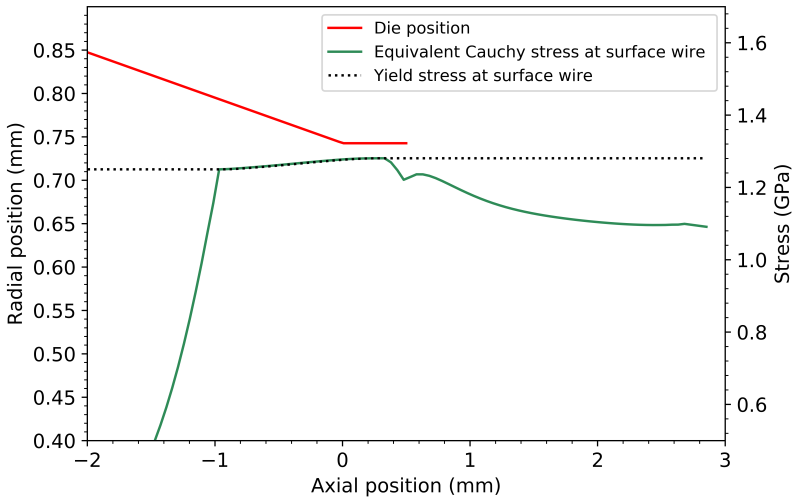

Figure 5: Equivalent Cauchy stress and yield stress of structure

Figure 6 demonstrates the radial displacement of the wire and the lubricant film thickness after reaching steady-state. The highest radial displacement is situated just before the narrow gap between wire and die. When the wire leaves the die, the wire is exposed to a limited elastic recovery as expected. Consequently, the minimum film thickness is situated at the outlet of the die.

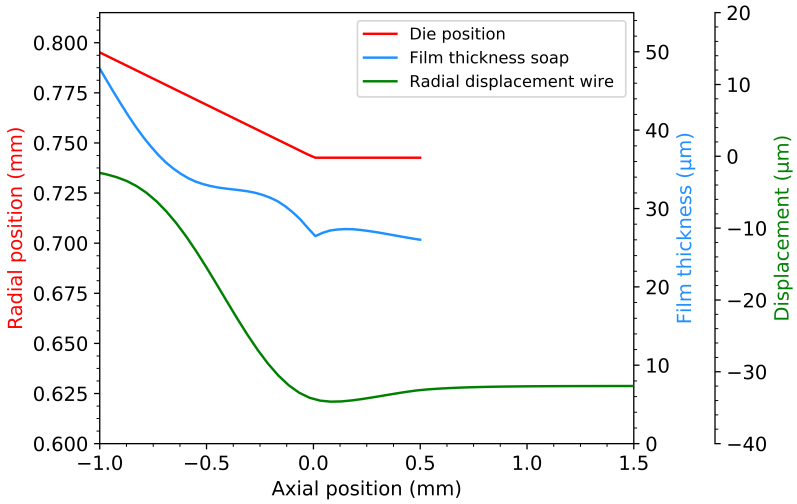

Figure 6: Radial displacement wire and lubricant film thickness

Figure 7 illustrates the pressure and shear-rate distribution of the lubricant on the interface at steady-state. The pressure distribution demonstrates a similar shape as the expected pressure distribution under a tapered land bearing [11]. The highest value is situated before the narrow gap. Furthermore, the minimum value of the shear stress distribution is situated nearby the pressure peak. The shear

stress increases significantly at the narrow gap and stays constant until the right end of the die.

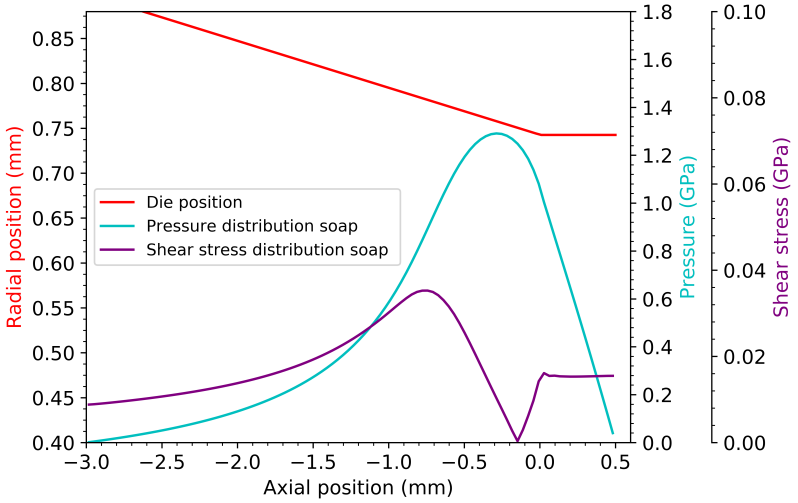

Figure 7: Pressure and shear stress distribution lubricant

Figure 8 displays the residuals of 6 time steps after reaching the steady-state condition. Each blue dot represents an FSI coupling iteration, with the calculated residual. For each time step, the FSI tolerance of 0.005 µm has been reached. The average number of FSI iterations per time step at steady-state is 4.5, which indicates a good performance of the IQN-ILS solver [9]. Moreover, 97.9% of the time is reserved for the structural calculation, while the fluid solver was 1.8% active and the FSI solver needs 0.3% calculation time.

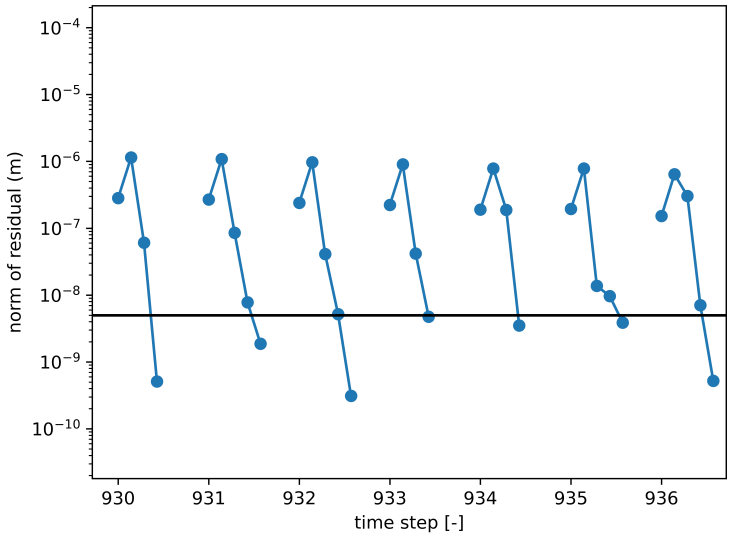

Figure 8: Residuals at steady-state

4 CONCLUSION

This paper presents a 2D axisymmetric FSI simulation of the dry wire drawing process with a no-slip condition on the sliding interface. Additionally, the implementation of the layering technique provides a reduction of the computational cost. However, combining layering and no-slip initially causes an oscillating behavior in the tangential velocity component at the interface, which is detrimental for the convergence of the FSI algorithm. To avoid these oscillations, a layer of cells is added each time step at the inlet of the structural domain. Additionally, the drawing force differs 8% compared with the slip condition at a maximum wire cross-section reduction of 9%. Consequently, the physical application of no-slip better predicts the energy consumption and the behavior of the drawing parameters. Furthermore, this case shows a converged solution with a good performance of the IQN-ILS solver. Remarkable is the large time consumption of the structural solver with respect to that of the fluid and FSI solvers, which requires further investigation.

The logical next step is focussed on the introduction of the piezo-viscous, thermal and shear thinning model of the lubricant.

5 ACKNOWLEDGMENTS

The authors gratefully acknowledge financial support from NV Bekaert SA, Belgium through Dr. Stijn De Pauw and VLAIO R&D project ViDB.

REFERENCES

[1] Skuric, V., De Jaeger, P., Jasak, H., Lubricated elastoplastic contact model for metal forming processes in OpenFOAM, *Comput. Fluids (2018)*, **172**: 226-240

[2] Hwang, J., Son, I., Yoo, J., Zargaran, A., Kim, N., Effect of reduction of area on microstructure and mechanical properties of twinning-induced plasticity steel during wire drawing, *Met. Mater. Int (2015)*, **21**: 815-822.

[3] Bair, S., Khonsari, M., Winer, W.O., High-pressure rheology of lubricants and limitations of the Reynolds equation, *Tribol. Int. (1998)*, **31**: 3323-3341.

[4] Vervaecke, M., Fauconnier, D., Degroote, J., OpenFOAM model of fluid-structure interaction in dry wire drawing, *The 8th European Congress on Computational Methods in Applied Sciences and Engineering, ECCOMAS Congress, Oslo* (2022).

[5] Holzmann, T., Mathematics, numerics, derivations and OpenFOAM, The basics for numerical simulations, *Holzmann CFD*, Release 7.0, URL https://Holzmann-cfd.de, DOI: 10.13140/RG.2.2.27193.36960.

[6] Cardiff, P., Tukovic, Z., De Jaeger, P., Clancy, M., Ivankovic, A., A Lagrangian cell-centred finite volume method for metal forming simulation, *Int. J. Numer. Meth. Engng (2017)*, **109**: 1777-1803.

[7] Jasak, H., Tukovic, Z., Dynamic mesh handling in OpenFOAM applied to fluid-structure interaction simulations, *V European Conference on Computational Fluid Dynamics, ECCOMAS CFD, Lisbon* (2010).

[8] Degroote, J., Partitioned simulation of fluid-structure interaction, coupling black-box solvers with quasi-Newton techniques, *Arch. Comput. Methods. Eng. (2013)*, **20**: 185-238.

[9] Delaissé, N., Demeester, T., Fauconnier, D., Degroote, J., Surrogate-based acceleration of quasi-Newton techniques for fluid-structure interaction simulations, *Comput. Struct. (2021)*, **260**: 106720, pp.21.

[10] Breuer, M., De Nayer, G. Münsch, M., Gallinger, T., Wüchner, R., Fluid-structure interaction using a partitioned semi-implicit predictor-corrector coupling scheme for the application of large-eddy simulation, *J. Fluids Struct. (2011)*, **29**: 107-130.

[11] van Beek, A., Advanced Engineering Design, Lifetime performance and reliability, *TU Delft*, ISBN-10: 90-810406-1-8